

Origin and Quantitative Description of the NESSIAS Effect at Si Nanostructures

Dirk König,* Michael Frentzen, Daniel Hiller, Noël Wilck, Giovanni Di Santo, Luca Petaccia, Igor Piš, Federica Bondino, Elena Magnano, Joachim Mayer, Joachim Knoch, and Sean C. Smith


The electronic structure of SiO₂- versus Si₃N₄-coated low nanoscale intrinsic silicon (Si) shifts away from versus toward the vacuum level E_{vac} , originating from the Nanoscale Electronic Structure Shift Induced by Anions at Surfaces (NESSIAS). Using the quantum chemical properties of the elements involved to explain NESSIAS, an analytic parameter Λ is derived to predict the highest occupied energy level of Si nanocrystals (NCs) as verified by various hybrid-density functional calculations and NC sizes. First experimental data of Si nanowells (NWells) embedded in SiO₂ versus Si₃N₄ were measured by X-ray absorption spectroscopy in total fluorescence yield mode (XAS-TFY), complemented by ultraviolet photoelectron spectroscopy (UPS), characterizing their conduction band and valence band edge energies E_C and E_V , respectively. Scanning the valence band sub-structure over NWell thickness yields an accurate estimate of E_V shifted purely by spatial confinement, and thus the actual E_V shift due to NESSIAS. Offsets of $\Delta E_C = 0.56$ eV and $\Delta E_V = 0.89$ eV were obtained for 1.9 nm thick NWells in SiO₂ versus Si₃N₄, demonstrating an intrinsic Si type II homojunction. This p/n junction generated by NESSIAS eliminates any deteriorating impact of impurity dopants, offering undoped ultrasmall Si electronic devices with much reduced physical gate lengths and CMOS-compatible materials.

1. Introduction

Si NWells with a thickness of $d_{well} \leq ca. 3.3$ nm embedded in silicon dioxide (SiO₂) versus silicon nitride (Si₃N₄) show an electronic structure shift with respect to the vacuum energy level E_{vac} as measured by UPS and XAS-TFY.^[1–3] NWells embedded in SiO₂ (Si₃N₄) get shifted to higher (lower) binding energies, that is, away from (towards to) E_{vac} . This NESSIAS effect is caused by quantum chemical properties of the anions forming the dielectric which surrounds the low nanoscale Si. While the NESSIAS effect has been established in theory and experiment, its exact origin and quantitative description are still elusive. Here, we deliver a detailed quantum chemical explanation of the NESSIAS effect, complemented with its semi-quantitative description which serves to predict NESSIAS in low nanoscale intrinsic Si for a variety of anions in embedding/coating dielectrics. To this end, we provide

D. König, S. C. Smith
 Integrated Materials Design Lab (IMDL)
 The Australian National University
 Canberra, ACT 2601, Australia
 E-mail: solidstatedirk@gmail.com; dirk.koenig@anu.edu.au
 M. Frentzen, N. Wilck, J. Knoch
 Institute of Semiconductor Electronics (IHT)
 RWTH Aachen University
 52074 Aachen, Germany
 D. Hiller
 Institute of Applied Physics (IAP)
 Technische Universität Bergakademie Freiberg
 09599 Freiberg, Germany

G. D. Santo, L. Petaccia
 Elettra Sincrotrone Trieste
 Strada Statale 14 km 163.5, Trieste 34149, Italy
 I. Piš, F. Bondino, E. Magnano
 IOM-CNR, Istituto Officina dei Materiali
 Area Science Park S.S. 14 km 163.5, Trieste 34149, Italy
 E. Magnano
 Department of Physics
 University of Johannesburg
 PO Box 524, Auckland Park 2006, South Africa
 J. Mayer
 Ernst-Ruska Centre for Microscopy and Spectroscopy with Electrons
 RWTH Aachen University
 52074 Aachen, Germany
 S. C. Smith
 Department of Applied Mathematics
 Research School of Physics and Engineering, The Australian National University
 Canberra, ACT 2601, Australia

 The ORCID identification number(s) for the author(s) of this article can be found under <https://doi.org/10.1002/apxr.202200065>

© 2023 The Authors. Advanced Physics Research published by Wiley-VCH GmbH. This is an open access article under the terms of the Creative Commons Attribution License, which permits use, distribution and reproduction in any medium, provided the original work is properly cited.

DOI: 10.1002/apxr.202200065

experimental evidence and details of the quantum-chemical concept which leads to the NESSIAS effect.

The NESSIAS effect induces a p/n junction on semiconductor nanostructures such as fins, nanowires (NWires), or NCs by enabling an electron flooding of the nanostructure when coated with SiO₂,^[3] or a virtually complete electron drainage from the nanostructure when coated with Si₃N₄,^[1,2] introducing a high density of holes into the nanovolume by the latter process. This re-arrangement of charge carrier densities has far-reaching consequences for semiconductor devices in very large scale integration (VLSI), ultra-low power and cryo-electronics. Spatial fluctuations of dopant densities, out-diffusion and self-purification impose a size limit onto VLSI devices as evident from *physical* gate lengths hovering around 20 nm since ca. 2014.^[4] With thermal dopant ionization not required, junctions induced by the NESSIAS effect should remain fully functional down to extremely low temperatures as useful for peripheral electronics in qbit manipulation.^[5]

The detection of the NESSIAS in low nanoscale intrinsic Si requires an absolute assignment of energies to E_{vac} , combined with elaborate UPS and XAS-TFY measurements and refined data processing for improved signal-to-noise ratios.^[1–3] To this end, the structures under investigation have to be in the range of the NESSIAS impact length. Many published Density Functional Theory (DFT) calculations^[6–9] lack an energy assignment on an absolute scale. Possibly identical low nanoscale intrinsic Si NWell systems near the low end of the one-digit nm range embedded in different dielectrics pose a challenge in experiment. The common perception of Si₃N₄ as an inferior dielectric on grounds of interface defect density^[10] and its more complex technology as opposed to SiO₂^[11] are likely reasons for the literature on low nanoscale Si embedded in or coated with Si₃N₄ being rather scarce. Indeed, standard Si₃N₄ has an interface defect density to low nanoscale Si which exceeds values of SiO₂/Si interfaces *ca.* 13-fold,^[10,12,13] though refined preparation techniques for high-quality H-passivated Si₃N₄-coatings rival trap densities on SiO₂/Si interfaces.^[14] This complex situation may explain why the NESSIAS might have been overlooked in the past.

We deliver a phenomenological and qualitative explanation of the NESSIAS effect in Section 2.1, resorting to quantum chemical properties of involved chemical elements. In Section 2.2, we derive an analytic parameter Λ of the NESSIAS effect to describe the energy of the highest occupied molecular orbital (HOMO) E_{HOMO} as a function of anion-specific quantum chemical properties combined with the charge of these main anions q_{main} of the ligand groups attached to Si NCs. In Section 2.3, we test Λ with a variety of density functionals (DFs) and most anionic elements of the first and second row of the periodic table with respect to Si, subject to the availability of experimental quantum chemical data. Our discussion is complemented with synchrotron data in Section 2.4. Since the electronic structure of NWells shifts as a function of quantum confinement, it is essential to separate this phenomenon induced by a *spatial* limit from the NESSIAS brought about by the quantum-chemical nature of embedding dielectric versus Si. To this end, we evaluate our results from synchrotron UPS measurements in Section 2.4.2, revealing substructures of the valence band which serve to estimate the actual quantum confinement. This true quantum confinement is revealed by the shift of the valence band (VB) edge to higher bind-

ing energies as a sole function of NWell thickness, occurring in all samples irrespective of the embedding dielectric. We use this VB edge as a reference level to estimate the *actual* NESSIAS as per embedding dielectric in the quantum confinement regime. Next, we evaluate our experimental data of the VB and conduction band edges as measured by synchrotron XAS-TFY in Section 2.4.3, establishing the link between bulk Si and SiO₂ versus Si₃N₄ as given by ultrathin Si NWells coated with the respective dielectric. Section 3 delivers a conclusion.

2. Results and Discussion

2.1. Qualitative Explanation of the NESSIAS Effect

When a common boundary between two different solids with a bandgap is formed, an interface charge transfer occurs,^[15] generating an interface dipole which may shift the electron work function of both materials with respect to the intrinsic solid-vacuum interface.^[15,16] The solid which accumulates extrinsic electrons experiences an electronic structure shift to lower binding energies E_{bind} , hence to E_{vac} , the other solid which provides the electronic charge experiences an electronic structure shift in the opposite direction. When low nanoscale intrinsic Si is coated with one atomic monolayer (1ML) SiO₂ or Si₃N₄, the interface charge transfer provides about the same amount of electrons to O and N as main interface anions,^[2] see to Supporting Information. We would thus expect a nearly identical shift of the low nanoscale intrinsic Si electronic structure in accord with interface dipole theory.

However, measurements of Si NCs^[17] and nanowells (NWells),^[1–3] and DFT calculations of Si NCs^[2,18,19] and nanowires (NWires)^[1] show a very different behavior. The Supporting Information lists energies of the lowest unoccupied MO (LUMO) E_{LUMO} , and E_{HOMO} of Si NCs together with the cumulative charge of the interface charge transfer $\sum q_{ICT}$ transferred from such Si NCs into the dielectric. These data show that E_{LUMO} and E_{HOMO} of Si NCs coated with SiO₂ (Si₃N₄) experience a shift to higher (lower) E_{bind} . The apparent contradiction to interface dipole theory can be resolved when looking at the quantum chemical properties of the chemical elements involved. Such elements are Si as the cation providing electrons, and in particular N or O as the anion receiving such electrons. Relevant properties of the anions are the electronegativity and resulting ionicity of bond to Si, the ionization energy E_{ion} , the electron affinity for the neutral anion X^0 , and the electron affinity of the anion ionized with one electron X^- , see **Table 1**. We focus on N and O as anions to explain the origin of the NESSIAS effect.

Table 1 shows that N has a much more positive X^0 and still more positive X^- than O, while its ionicity of bond to Si is *ca.* 2/3 of the value O provides. This lower ionicity of bond and an associated lower charge of the interface charge transfer *per bond* q_{ICT} is nearly cancelled out by N in Si₃N₄ having 3/2 interface bonds to Si on average due to its trivalent configuration. Thus, values of the cumulative charge transferred to the main anions $\sum q_{ICT}$ for NCs of same size embedded into 1 ML SiO₂- versus Si₃N₄ are nearly equal.

Evaluating $\sum q_{ICT}$, E_{HOMO} , and E_{LUMO} (Supporting Information) shows that the NESSIAS remains in saturation (i.e., at maximum strength) for NCs embedded in 1 ML SiO₂ up to $d_{NC} = 1.85$

Table 1. Electronegativity (EN) of the ligand elements, resulting ionicity of bond (IOB) to Si, first ionization energy (E_{ion}), electron affinity in neutral state (X^0) and ionized with one negative charge (X^-). Values are from^[20] apart from X^- .

Element	EN ^{a)}	IOB to Si [%]	E_{ion} [eV]	X^0 [eV]	X^- [Reference] [eV]
Si	1.74	0	8.15	-1.38	
B	2.01	2	8.30	-0.28	+5.58 [21] ^{b)}
H	2.20	5	13.60	-0.76	+5.85 [22] ^{c)}
C	2.50	13	11.26	-1.26	+9.03 [22] ^{c)}
N	3.07	36	14.53	+0.07	+8.30 [23] ^{b)}
O	3.50	54	13.36	-1.46	+8.03 [24] ^{c)}
F	4.10	75	17.42	-3.40	+7.69 [22] ^{c)}
S	2.44	12	10.36	-2.08	+6.12 [22] ^{c)}

a) Allred & Rochow; b) measured; c) calculated.

nm ($\text{Si}_{165}(\text{OH})_{100}$). The $\text{Si}_{286}(\text{OH})_{144}$ approximant with $d_{\text{NC}} = 2.2$ nm shows the onset of E_{HOMO} moving toward E_{vac} which indicates the size limit limit of NESSIAS saturation. For the $\text{Si}_{455}(\text{OH})_{196}$ approximant with $d_{\text{NC}} = 2.6$ nm, the NESSIAS is yet weaker as is evident from another slight shift of E_{HOMO} and E_{LUMO} toward E_{vac} . Increasing the embedding from 1 to 1.5 ML SiO_2 marginally increases $\sum q_{\text{ICT}}$ per NC size and pushes the size regime where the NESSIAS becomes unsaturated beyond $d_{\text{NC}} = 2.2$ nm.

Although $\sum q_{\text{ICT}}$ is lower for Si NCs embedded in 1 ML Si_3N_4 versus embedding in 1 ML SiO_2 , no NESSIAS saturation occurs for $d_{\text{NC}} \leq 2.6$ nm as evident from E_{HOMO} and E_{LUMO} not moving away from E_{vac} to higher E_{bind} . When going from 1 to 1.5 ML Si_3N_4 -embedding, the NC is surrounded by more N atoms in a thicker Si_3N_4 layer. Counterintuitively, $\sum q_{\text{ICT}}$ drops notably, and E_{HOMO} and E_{LUMO} slightly move to lower E_{bind} which contradicts the presence of significantly more N atoms.

We thus can state for SiO_2 -embedding that the NESSIAS effect looks rather spatially compact and comes out of saturation fairly quickly with increasing system size of low nanoscale intrinsic Si. For Si_3N_4 -embedding, the NESSIAS effect appears to be spatially distributed and the electronic shift is rather smooth, extending over a wider size range of low nanoscale intrinsic Si. In order to understand this peculiar electronic structure, we look at a sketch combining spatial atomic orbital distribution and energy levels, see Figure 1.

Arguably, the delocalizing impact of N versus the localizing impact of O onto their acquired electronic charge is the key to the NESSIAS effect. We can interpret a decreased $\sum q_{\text{ICT}}$ for N which decreased further for a thicker Si_3N_4 layer as a partial reflection of q_{ICT} back into the intrinsic Si. These observations are confirmed by experimental results of Si_3N_4 - versus SiO_2 -embedded Si NWells, see Section 2.4.2 and Figure 8. The atomistic nature of the NESSIAS implies a short impact length in accord with other near-field effects such as significant electron tunneling.^[25] For intrinsic Si, the extension of the NESSIAS is ca. 1.3 to 1.8 nm per plane interface.^[1-3]

2.2. Analytic Relation of the NESSIAS Effect with the HOMO Energy

We consider interfaces constituted by single bonds, such as between Si/SiO_2 and $\text{Si}/\text{Si}_3\text{N}_4$. A detailed derivation of the equa-

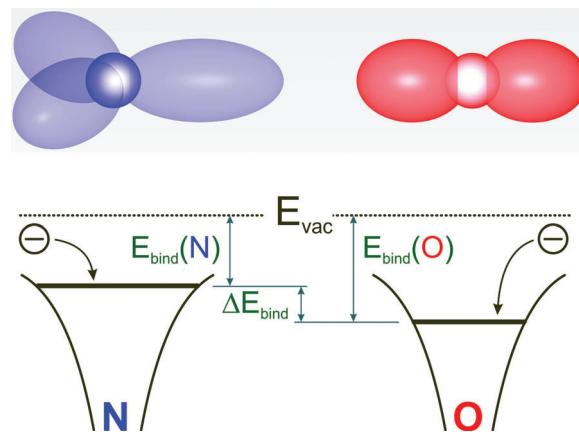


Figure 1. Relevant quantum chemical properties of N and O shown in spatial space and energy. The top graph shows the spatial extension of frontier occupied hybrid atomic orbitals. N and in particular O attract electrons from afar due to their high electronegativity. The key difference between N and O is given by the local electronic properties: N delocalizes extrinsic electrons due to its positive X^0 and X^- ; O localizes such electrons with its more negative X^0 and X^- . The bottom graph shows the consequence in the energy picture: frontier atomic orbitals (and their anti-/non-bonding counterparts) shift to lower E_{bind} for Si_3N_4 -embedding, while frontier atomic orbitals for SiO_2 -embedding shift to higher E_{bind} .

tions below and the use E_{ion} , X^0 and X^- of the interface main anion of the considered ligand group together with the average charge of the main anion $q_{\text{main}}^{\text{avg}}$ as boundary values are given in the Supporting Information. Here, we focus on results to express E_{HOMO} with its dependence on the nature of interface bonds as a function of the parameter $\Lambda_{\text{main}}^{q(\text{main})}$. The average charge of the main anion constituting the ligands to Si NCs $q_{\text{main}}^{\text{avg}}$ is derived from DFT calculations and presents the only non-analytic input to $\Lambda_{\text{main}}^{q(\text{main})}$. We calculate the parameter for a negative charge transfer to the main anion – which is the most likely case –

$$\Lambda_{\text{main}}^{q(\text{main})} = (1 - |q_{\text{main}}^{\text{avg}}|^3)X_{\text{main}}^0 + \underbrace{|q_{\text{main}}^{\text{avg}}|^3 X_{\text{main}}^-}_{\text{due to negative ionization}} \quad \forall q_{\text{main}}^{\text{avg}} \leq 0 \quad (1)$$

and a positive charge transfer to the main anion of the ligand (or dielectric)

$$\Lambda_{\text{main}}^{q(\text{main})} = (1 - |q_{\text{main}}^{\text{avg}}|^3)X_{\text{main}}^0 - \underbrace{|q_{\text{main}}^{\text{avg}}|^3 E_{\text{ion,main}}}_{\text{due to positive ionization}} \quad \forall q_{\text{main}}^{\text{avg}} \geq 0. \quad (2)$$

The parameter $\Lambda_{\text{main}}^{q(\text{main})}$ describes the binding energy of the interface bond and is proportional to E_{HOMO} , or the energy of the valence band maximum E_V for sufficiently large low nanoscale intrinsic Si systems like NWells evaluated in Section 2.4.2. We can thus use $\Lambda_{\text{main}}^{q(\text{main})}$ to predict the NESSIAS as a function of the embedding dielectric, thereby providing optimum combinations of Si and dielectrics per design to meet the desired functionality of VLSI electronic devices as briefly discussed below.

Figure 2 shows the result of Equations 1 and 2, together with the data points of all ligands used in DFT calculations of Si_{35} NCs

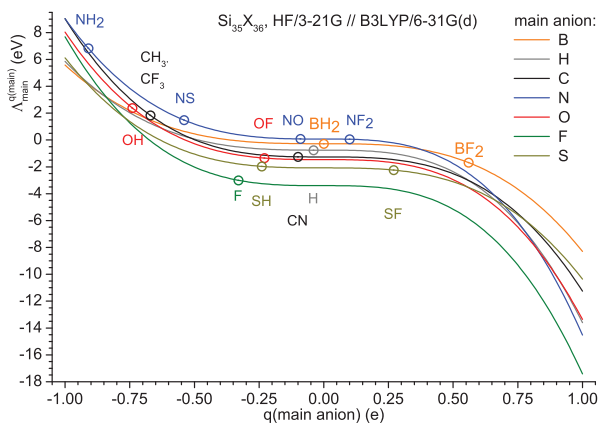


Figure 2. The parameter $\Lambda_{\text{main}}^{q(\text{main})}$ shown as a function of transferred charge from intrinsic Si to main anion $q(\text{main})$ for all anionic terminations and their possible outer terminations, see Table 1. $\Lambda_{\text{main}}^{q(\text{main})}$ for $\text{Si}_{35}\text{X}_{36}$ ($X =$ ligand) is shown per main anion for $q(\text{main}) \in [-1; +1]$, with the respective data point per functional group termination derived from q_{main} (DFT), see Figure 4 for corresponding data on electronic structure and $\Lambda_{\text{main}}^{q(\text{main})}$. The difference in $\Lambda_{\text{main}}^{q(\text{main})}$ as per main anion which describes the respective dielectric provides an estimate for the strength of the VB offset ΔE_V between accordingly coated low nanoscale intrinsic Si sections, and can be used for VLSI device design.

(Section 2.3). Embedding in SiO_2 versus Si_3N_4 is indeed a good choice for a maximum NESSIAS. Coating low nanoscale intrinsic Si with Fluoride is even more attractive for a maximum electronic structure shift to higher E_{bind} as evident from the bigger difference in $\Lambda_{\text{main}}^{q(\text{main})}$ to Si_3N_4 -embedding. Such differences as per embedding dielectric of low nanoscale intrinsic Si are useful to predict the adequate combination of dielectrics to arrive at type II homojunctions required for VLSI field effect transistors (FETs), for example, using SiO_2 - and Si_3N_4 -embedding, or potentially at band-to-band tunneling (BTBT) FET devices by replacing SiO_2 - with Fluoride-embedding.

Since Si and other semiconductors have a significant interatomic charge transfer, the NESSIAS effect will not be limited to a few atomic MLs within intrinsic low nanoscale Si, providing the basis for its use in VLSI electronics. Within the dielectric, a charge transfer over more than four Si-X ($X = \text{O}, \text{N}$) MLs becomes unnotable in particular for SiO_2 embedding^[1,2] because of the strong polar nature of the bonds and immobility of local charges due to charge localization and a rather wide bandgap of SiO_2 and Si_3N_4 .

2.3. Verification of the Analytic Relation with DFT Simulations

DFT approximants consist of NCs fully terminated with one ligand and type. The main anion forms the center of the ligand and the interface bond to the NC. Relevant properties of main anions are listed in Table 1. **Figure 3** shows examples of NCs calculated by DFT. In **Figure 4**, the dependence $E_{\text{HOMO}} \propto \Lambda_{\text{main}}^{q(\text{main})}$ can be clearly seen for Si_{35} NCs with a diameter of $d_{\text{NC}} = 1.1$ nm as a function of their surface termination, where ligands are grouped in accord with their main anion, and specific outer terminations where applicable, arranged for increasing electronegativity from left to

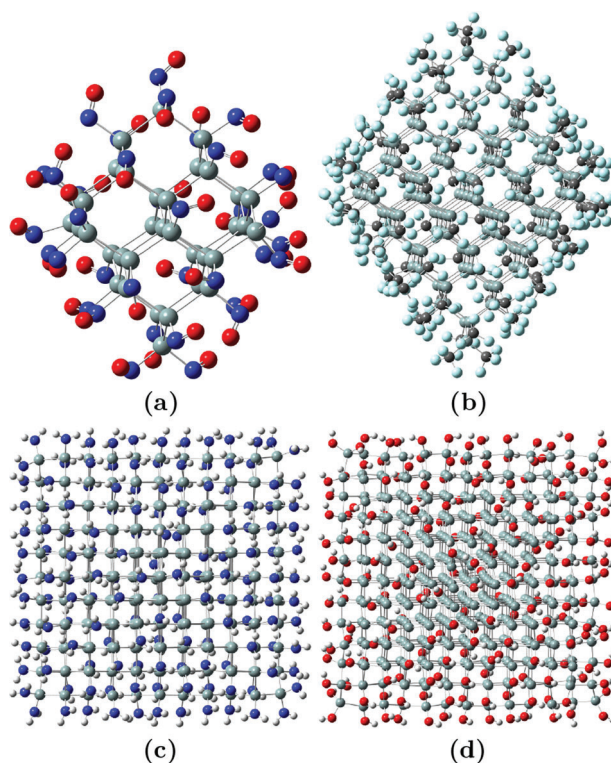


Figure 3. Examples of structurally optimized approximants of which DFT data are shown in Figures 2 and 4 and in the Supporting Information: a) $\text{Si}_{35}(\text{NO})_{36}$, b) $\text{Si}_{165}(\text{CF}_3)_{100}$, shown along the $\langle 110 \rangle$ vector class, and c) $\text{Si}_{286}(\text{NH}_2)_{144}$, and d) $\text{Si}_{455}(\text{OH})_{196}$, shown along the $\langle 001 \rangle$ vector class. Atom colors are white (H), anthracite (C), blue (N), red (O), pastel green (F), and gray (Si). Further Data on other DFs and NC sizes can be found in the Supporting Information.

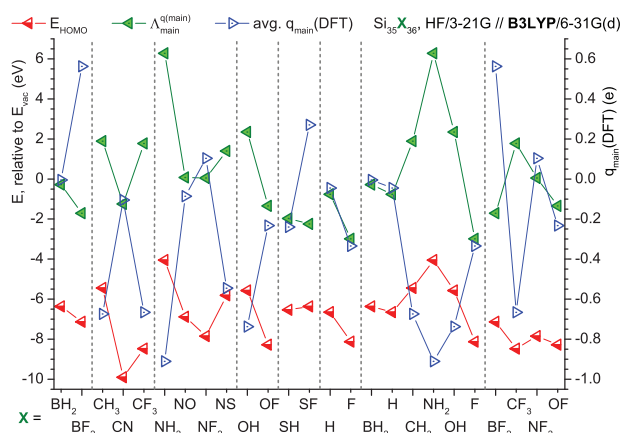


Figure 4. Energy E_{HOMO} (red symbols) with $\Lambda_{\text{main}}^{q(\text{main})}$ (green symbols) shown relative to E_{vac} , referring to left y-axis. The average charge of the main anions $q(\text{main})$ (blue symbols) refers to the right y-axis. All values were calculated for $\text{Si}_{35}\text{X}_{36}$ NCs (1.1 nm size, $X = \text{BH}_2, \text{BF}_2$, etc.) as a function of complete surface termination noted at the abscissa, with main anions B, C, H, N, O, F, and S. As indicated in the legend, the structural optimization // electronic structure calculations were carried out with HF/3-21G // B3LYP/6-31G(d), see text for details. More data obtained by the CAM-B3LYP and HSE06 DFs for Si_{35} , and for Si NCs up to 2.6 nm size (Si_{455}) are available in the Supporting Information.

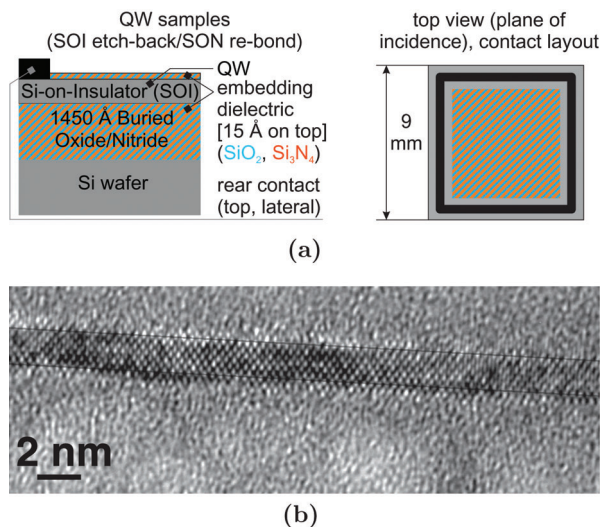


Figure 5. Layout of Si_3N_4 - and SiO_2 -embedded Si NWell samples for synchrotron UPS and XAS-TFY, shown in X-section and top view a). X-section view of 1.7 nm (001)-Si NWell in Si_3N_4 seen along the $\langle 110 \rangle$ vector class as obtained by TEM b). Semi-transparent black lines show interfaces to adjacent Si_3N_4 from where the NWell thickness was determined.

right. Recently, H-terminated 1.1 nm size Si NCs were processed by a top-down design.^[26] For Si NCs fully terminated with BF_2 , CF_3 , NF_2 , and OF ligands, $\Lambda_{\text{main}}^{q(\text{main})}$ slightly deviates from E_{HOMO} as discussed in the Supporting Information. All other terminations are described accurately by $\Lambda_{\text{main}}^{q(\text{main})} \propto E_{\text{HOMO}}$ (green and red symbols, respectively, in Figure 4).

We extended calculations of Si_{35} NCs to other hybrid DFs, the Heyd–Scuseria–Ernzerhof DF with its 2006 parametrization (HSE06),^[27] and the B3LYP DF complemented with the Coulomb Attenuation Method (CAM-B3LYP).^[28] Detailed results of such calculations are listed in the Supporting Information, further corroborating the accuracy of $\Lambda_{\text{main}}^{q(\text{main})}$ in predicting E_{HOMO} .

2.4. Details of the NESSIAS Effect in Si NWells from Experiment

2.4.1. Sample Layout

Figure 5a shows the sample layout used in synchrotron XAS-TFY. The sample layout used for UPS is virtually identical, see Figure 2 in Ref. [2]. Layer thicknesses were measured by ellipsometry and calibrated on selected samples by transmission electron microscopy (TEM), see Figure 5b. All NWells were processed from Silicon-on-Insulator (SOI) with p-type doping of 1×10^{15} to $1 \times 10^{16} \text{ cm}^{-3}$, and an interstitial oxygen (O_i) concentration of 1 to $2 \times 10^{17} \text{ cm}^{-3}$ equivalent to 2 to 4 ppm O_i in Si^[29,30] as required for VLSI processing. As surface roughness, we obtained a standard deviation of $\sigma \approx \pm 0.2 \text{ nm}$ from the nominal d_{NWell} values as derived from TEM X-section images showing $\sigma \approx \pm 1 \{001\}$ Si ML, see Figure 5b and to error bars in Figure 8.

2.4.2. Calibrating the NESSIAS by Measuring the Intrinsic Valence Band Edge with Synchrotron UPS

First data of SiO_2 - and Si_3N_4 -embedded Si NWells were obtained by measuring the VB maximum (leading edge) of bulk Si and em-

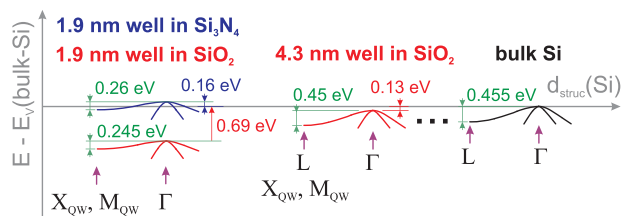


Figure 6. Sketch of the electronic structure of the VB top with $\Delta E_V^{\text{VanHove}}$, evolving with decreasing d_{Well} . Subbands are shown for bulk Si (black), for NWells in SiO_2 (red), and for NWells in Si_3N_4 (blue). Values of the VB maximum shifting relative to the VB edge of bulk Si were taken from the respective least residual fit in Figure 8. Values of $\Delta E_V^{\text{VanHove}}$ are shown in dark green, see to Figure 7, and to Supporting Information for more details.

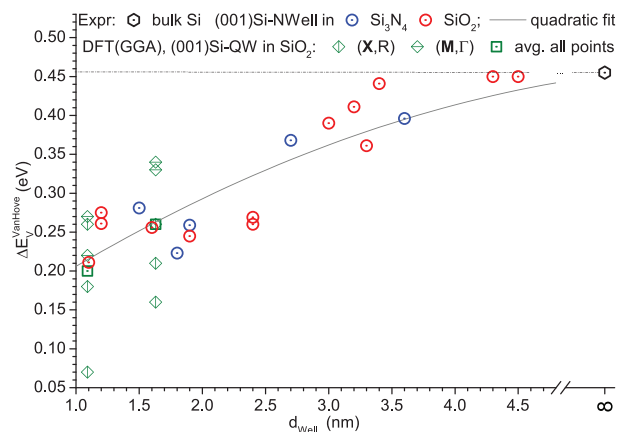


Figure 7. Energy difference between VB-DOS extrema at Γ point and adjacent Van Hove singularities $\Delta E_V^{\text{VanHove}}$ as function of d_{Well} embedded in SiO_2 (red dots) and in Si_3N_4 (blue dots). The gray line is a quadratic-hyperbolic least residuals fit, the black hexagonal symbol shows the bulk value of $\Delta E_V^{\text{VanHove}}$; please observe abscissa break. Green symbols denote Van Hove singularities for Si NWells in SiO_2 with $d_{\text{Well}} = 1.09$ and 1.63 nm , embedded in 1.92 nm thick SiO_2 barriers as calculated by DFT with periodic boundary conditions.^[34] Small rhomboid symbols show local Van Hove singularities per k-point, the big square symbol per d_{Well} shows their average value. For details on UPS measurement and data retrieval from published DFT calculations, see to Supporting Information.

bedded Si NWells using scan ensembles of synchrotron UPS^[1–3] with their statistic data, whereby the VB maximum is located at Γ point; $E_V = E_V^\Gamma$. We now discuss the fine structure of UPS spectra, revealing a sub-edge which can be assigned to the Van Hove singularity of bulk Si at the L point in the Brillouin zone with its energy E_V^L .^[31,32] For NWells with $d_{\text{Well}} \leq 5 \text{ nm}$, the VB subband structure becomes increasingly perturbed by quantum confinement. An assignment of subband Van Hove singularities near E_V becomes a function of d_{Well} and of specific high symmetry points in the electronic DOS along non-orthogonal \mathbf{k} -directions of the NWell plane, in particular X and M, see to Supporting Information. **Figure 6** illustrates the change in VB electronic structure with the shrinking size of low nanoscale intrinsic Si using experimentally derived values. We focus on the energy offset between Γ and L point for bulk Si, and between Γ and X, M points for thin NWells, generally expressed by the term $\Delta E_V^{\text{VanHove}}$.

Figure 7 shows that $\Delta E_V^{\text{VanHove}}$ does not depend on the embedding dielectric as should be the case for a pure quantum con-

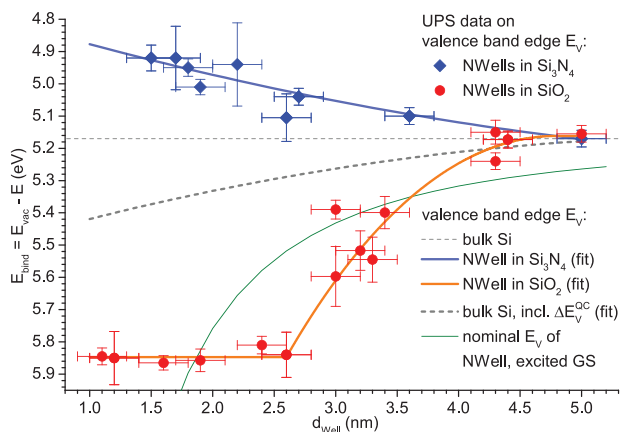


Figure 8. Synchrotron UPS data of the VB maxima of Si NWells embedded in SiO₂ (red symbols) and Si₃N₄ (blue symbols). Error bars show standard deviations in thickness and energy. Orange and light blue lines provide a least square residual fit to $E_V(d_{\text{Well}})$ for SiO₂- and Si₃N₄-embedding, respectively. The thin dashed gray line shows E_V of bulk Si. The thick dashed gray line shows E_V with intrinsic quantum confinement $E_V^{\text{QC}}(d_{\text{Well}})$, see text and Figure 7 for details. The green line shows E_V of the nanowell for photon absorption (including exciton binding energy, excluding lattice relaxation; unrelaxed excited state) as per existing theory.

finement phenomenon with sufficiently high potential walls (i.e., band offsets between respective bulk phases),^[33] cf. Figure 10a. When quantum confinement sets in with decreasing d_{Well} , the energy offset between VB-DOS extrema at Γ and adjacent Van Hove singularities $\Delta E_V^{\text{VanHove}}$ diminishes as E_V^{Γ} is shifted to higher binding energies. Since the adjacent Van Hove singularities already have higher binding energies with respect to the VB maximum, they do not experience a notable energy shift due to quantum confinement even for the minimum energetic distance of $\Delta E_V^{\text{VanHove}} \approx 0.2$ eV for NWells with $d_{\text{Well}} = 1.1$ nm, see Figure 7. We can, therefore, take $\Delta E_V^{\text{VanHove}}$ as a good estimate for the shift of $E_V^{\Gamma} = E_V$ to higher binding energies due to quantum confinement only. Interestingly, DFT-GGA calculations of Si NWell superlattices (SLs) with 1.9 nm thick SiO₂ barriers^[34] yield very similar values of $\Delta E_V^{\text{VanHove}}(d_{\text{Well}})$, cf. Figure 7 and discussion in the Supporting Information. We introduce a VB maximum as a function of NWell thickness,

$$E_V^{\text{QC}}(d_{\text{Well}}) = E_V(\text{bulk Si}) + [E_V^{\Gamma}(\text{bulk Si}) - E_V^{\text{L}}(\text{bulk Si})] - \Delta E_V^{\text{VanHove}} = 5.17 \text{ eV} + 0.455 \text{ eV} - \Delta E_V^{\text{VanHove}} \quad (3)$$

In Figure 7, a quadratic-hyperbolic least residuals fit was used in accord with quantum confinement theory^[33] to estimate the shift of E_V as a function of d_{Well} .

We present all UPS data together with $E_V^{\text{QC}}(d_{\text{Well}})$ in Figure 8. The energy offset due to the NESSIAS as per embedding dielectric is clearly visible, saturating for SiO₂-embedding for $d_{\text{Well}} \leq 2.6$ nm, while steadily growing with decreasing d_{Well} for Si₃N₄-embedding. The VB offset between 1.6 nm thick Si NWells coated with Si₃N₄ versus SiO₂ is $\Delta E_V \approx 0.95$ eV, facilitating charge carrier separation on a massive scale in analogy to a steep p/n junction induced by impurity doping. Apparently, such experimen-

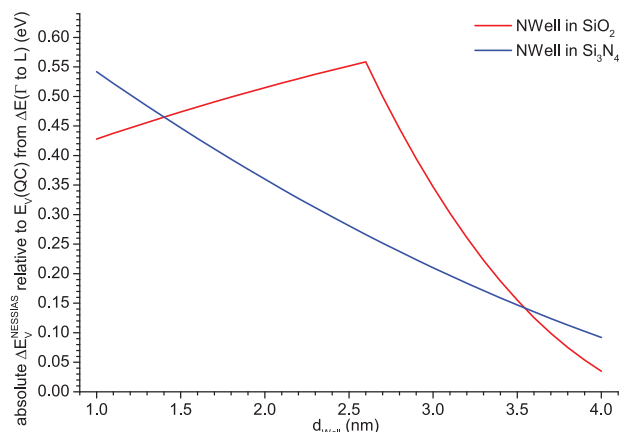


Figure 9. Absolute values of $\Delta E_V^{\text{NESSIAS}}$ as a function of d_{Well} relative to $E_V^{\text{QC}}(d_{\text{Well}})$, using the least square residual fits of VB edges of Figure 8. The NESSIAS becomes saturated for NWells in SiO₂ around $d_{\text{Well}} = 2.6$ nm, but not for $d_{\text{Well}} \geq 1.0$ nm for NWells in Si₃N₄, see text for further discussion.

tal data differ considerably from the E_V for bulk Si (thin dashed gray line) for $d_{\text{Well}} \leq 3.5$ nm. We further note that the conventional quantum confinement description of $E_V(d_{\text{Well}})$ of the excited ground state^[33] – that is, the ground state E_V minus the partition of the exciton binding energy residing with the hole – deviates notably from both, $E_V(d_{\text{Well}})$ without the NESSIAS effect as derived above (Figure 7 and Equation 3), and $E_V(d_{\text{Well}})$ as measured for Si NWells embedded in Si₃N₄ and SiO₂. Before discussing the full electronic structure of embedded Si NWells with experimental data, we revisit the discussion of the quantitative NESSIAS impact due to Si₃N₄ versus SiO₂.

With $E_V^{\text{QC}}(d_{\text{Well}})$, we have a true reference level to investigate on a quantitative base how the NESSIAS affects Si NWells per embedding dielectric. To that effect, we calculate the absolute value of the difference between $E_V^{\text{QC}}(d_{\text{Well}})$ and the VB maximum $E_V(d_{\text{Well}})$ per embedding dielectric, viz. $|\Delta E_V^{\text{NESSIAS}}| = |E_V^{\text{QC}}(d_{\text{Well}}) - E_V(d_{\text{Well}})|$ cf. Figure 9.

As already emerging from Figure 8, $|\Delta E_V^{\text{NESSIAS}}|$ becomes saturated for $d_{\text{Well}} \leq 2.6$ nm for NWells in SiO₂. The strong localization of extrinsic electrons from the NWell at the O atoms in SiO₂ has two effects. Due to the small localization volume which is limited to the immediate proximity of O atoms, see Section 2.1, these atoms undergo electrostatic screening. Thereby, the interface charge transfer from the NWell to SiO₂ is self-limiting. The NWell undergoes a rather strong positive ionization, increasing the attractive Coulomb force which works against the interface charge transfer. Together with the screened O atoms, the cumulative charge of the interface charge transfer $\sum q_{\text{ICT}}$ thus decreases for $d_{\text{Well}} < 2.6$ nm, whereby its partition per Si NWell atom still increases. The latter statement is straightforward to see when comparing $|\Delta E_V^{\text{NESSIAS}}|$ of $d_{\text{Well}} = 2.6$ nm with its value at half the NWell thickness. There, $|\Delta E_V^{\text{NESSIAS}}|$ decreased from its maximum of 0.56 eV at $d_{\text{Well}} = 2.6$ nm not by about 0.28 eV as would be the case for a constant NWell ionization, but by a mere 0.10 eV, accounting for a further increase of the positive ionization per Si NWell atom. We note, though, that the electronic DOS of the VB over energy is not constant. Further decrease in $|\Delta E_V^{\text{NESSIAS}}|$ may

occur due to an increased DOS at the energy where $E_V^{QC}(d_{well})$ resides. The situation is very different for Si_3N_4 -embedding, where $|\Delta E_V^{NESSIAS}|$ is constantly increasing for a decreasing d_{well} , getting close to the saturation limit of SiO_2 -embedding. This behavior is in accord with the quantum-chemical properties of N, see Section 2.1. It is uncertain whether we can proceed to Si_3N_4 -embedded NWells with $d_{well} < 1.1$ nm to find a saturation limit in experiment should it exist. What we do know from experiment is that the constant increase of $|\Delta E_V^{NESSIAS}|$ with decreasing d_{well} results from the electron-attractive, yet delocalizing nature of N which does not suffer from a saturation due to a much bigger volume which can be utilized by N to accommodate extrinsic electrons. As discussed in Section 2.1, this peculiar behavior also results in a part of the interface charge transfer to be reflected back into the NWell as a consequence of the decreased binding energy of extrinsic electrons at N atoms, thereby shifting the electronic structure of the NWell and low nanoscale intrinsic Si in general toward E_{vac} .

We have stated in Section 2.1 that 1 ML SiO_2 can keep the NESSIAS saturated for a ratio of low nanoscale intrinsic Si atoms per interface bond of $N_{IF}/N_{Si} = 196/455 \approx 0.43$ for Si NCs. Figure 8 shows that this saturation is left around $d_{well} = 2.6$ nm which corresponds to ca. 19 atomic ML of (001)Si or 38 Si atoms and eight interface bonds per unit cell area, resulting in $N_{IF}/N_{Si} = 8/38 \approx 0.21$. Assuming an exponential decay in charge transfer through SiO_2 when moving away from the interface, we arrive at the estimate of ca. 3 ML or 0.9 nm SiO_2 ^[1,17] after which the NESSIAS does not increase significantly anymore by increasing the thickness of SiO_2 . While this is good news for the VLSI technology where ultrathin SiO_2 layers are required to chemically passivate low nanoscale intrinsic Si and to establish the primary layer of gate dielectrics, there is little chance to extend a saturated NESSIAS in Si beyond $d_{well} = 2.6$ nm. For Si_3N_4 -embedding, the delocalizing impact of N yields to a NESSIAS smeared out over d_{well} , with no saturation present for $d_{well} \geq 1.5$ nm.

2.4.3. A First Glimpse on the Full NESSIAS Picture

We recently started to measure the energy of the conduction band edge E_C of Si NWells embedded in SiO_2 by means of X-ray Absorption Spectroscopy in Total Fluorescence Yield mode (XAS-TFY).^[3] An initial sample of a Si_3N_4 -coated NWell gave us a very first glimpse on the electronic structure of Si NWells of comparable thickness as a function of their embedding. We thus focus here on two NWell samples with $d_{well} = 1.9 \pm 0.2$ nm and the respective embedding. Details of other SiO_2 -coated NWells can be found in [3] and its supporting information, representative scans and statistical data of both samples used here can be found in the Supporting Information. The obtained experimental data for E_V and E_C are shown together with the bulk phases of Si, SiO_2 , and Si_3N_4 in Figure 10a. Figure 10b shows a combination of both NWell samples, with the resulting band diagram as per experimental data from Figure 10a. Obviously, we can induce a strong type II homojunction^[40] in low nanoscale intrinsic Si merely by coating with SiO_2 versus Si_3N_4 .

The band structures of bulk solids shown in Figure 10a yield to further insights into the NESSIAS effect. The band offsets between the bulk phases of Si and SiO_2 as well as Si and Si_3N_4 are

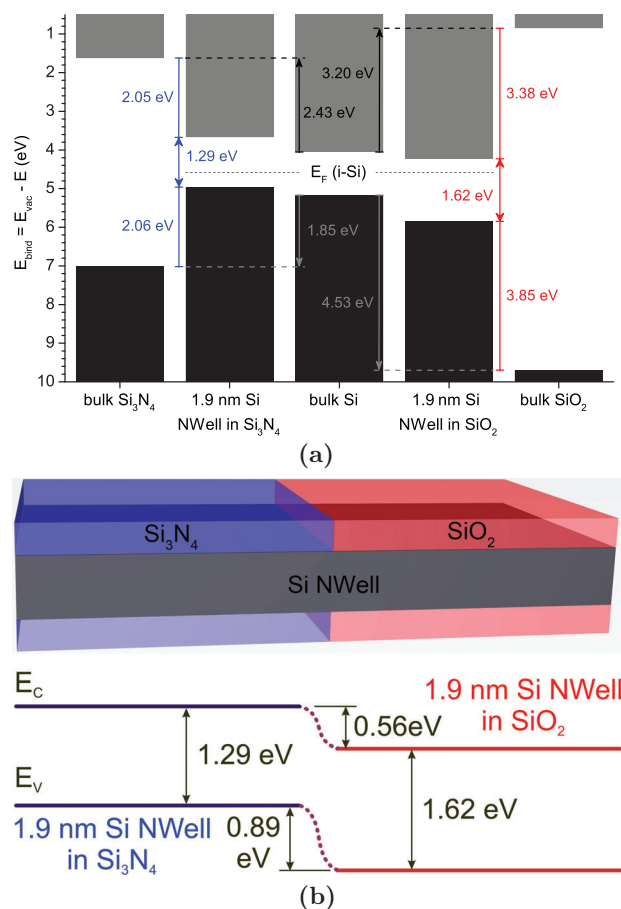


Figure 10. a) Regions of fundamental band gaps for – left to right – bulk Si_3N_4 ,^[1,35–37] a 1.9 nm Si-NWell in Si_3N_4 , intrinsic bulk Si,^[1,38] a 1.9 nm Si-NWell in SiO_2 ,^[1,37–39] and bulk SiO_2 .^[1,37–39] Band offsets to dielectrics are shown by labelled red (blue) lines for NWells in SiO_2 (Si_3N_4), and in gray/black for bulk Si. Band edges given contain values of bulk solids from experiment, data for NWells were obtained by UPS and XAS-TFY, see to text, to Supporting Information and to^[1–3] with respective supplements. b) Layer system comprising a 1.9 nm thick Si NWell coated with 1.0 nm Si_3N_4 and SiO_2 (top), and its band diagram with energies in units of eV (bottom), derived from experimental data in graph (a).

somewhat asymmetric. A strong shift of E_C , E_V to higher binding energies occurs for SiO_2 . For Si_3N_4 , we see a smaller shift to lower binding energies. Both observations are in accord with our discussion of O and N versus Si in Section 2.1. We thus can track the NESSIAS effect all the way to the bulk phase of the respective dielectric. As a consequence, the entire electronic structure of low nanoscale intrinsic Si such as a sufficiently thin NWell moves toward a more symmetric band offset with the respective dielectric when the NESSIAS effect becomes significant.

From above discussion, the question of a low nanoscale intrinsic Si size limit arises below which it starts to behave like the embedding dielectric to a degree where they depart from the properties of semiconducting Si. Further research efforts will be required to provide a thickness estimate around which the NESSIAS effect can be put to best use for technological applications from the viewpoint of low nanoscale intrinsic Si system size. Moreover, recent DFT calculations^[3] showed that other group

IV semiconductors such as C and Ge – and presumably their alloys SiC and SiGe – strongly respond to the NESSIAS, offering a much broader impact on VLSI device design beyond low nanoscale Si.

3. Conclusion

We quantitatively demonstrated that an energy shift of electronic states defining the conduction band and VB edge of low nanoscale intrinsic Si exists, being considerably different from commonly assumed energy positions. The underlying Nanoscale Electronic Structure Shift Induced by Anions at Surfaces (NESSIAS) is brought about by the embedding dielectric, whereby N in the form of Si_3N_4 and O in the form of SiO_2 are of particular scientific and technological interest. We explained the underlying quantum chemical processes of the NESSIAS which mainly reside with the anion of the dielectric, namely its ability to attract extrinsic electrons such as from low nanoscale intrinsic Si from afar (electronegativity defining the ionicity of bond to Si), and its ability to localize extrinsic electrons in its immediate vicinity (electron affinity X). Electronic states experience a shift to higher binding energies with O as an interface anion, while the delocalization of extrinsic electrons in the immediate vicinity of N reflects such states partly back to Si, lowering the binding energy for low nanoscale intrinsic Si systems. The NESSIAS thus results in an electronic structure shift toward (away from) E_{vac} for Si_3N_4 - (SiO_2 -) embedding. Hence, low nanoscale intrinsic Si systems like NWires^[3] or NWells can be flooded by holes (Si_3N_4 -coated) or electrons (SiO_2 -coated), a property which readily offers the formation of a type II (p/n) homojunction in low nanoscale intrinsic Si.

We introduced an analytic parameter as a function of the ionization of the main interface anion $\Lambda_{\text{main}}^{q(\text{main})}$ which correctly predicts the HOMO energy E_{HOMO} of the low nanoscale intrinsic Si system. This parameter is a function of the main interface anion presenting the coating dielectric. A verification of $\Lambda_{\text{main}}^{q(\text{main})}$ with three hybrid DFs showed its accuracy in predicting E_{HOMO} . As main anions to Si, we evaluated the entire first period of the periodic table and S, with all of these main anions terminated by all possible outer atoms to form ligands. Using $\Lambda_{\text{main}}^{q(\text{main})}$ to predict the NESSIAS as a function of the dielectric coating, we obtain optimum combinations of Si and dielectrics per design to meet the desired functionality of VLSI electronic devices.

Band edges of 1.9 nm thick Si NWells measured by UPS and XAS-TFY revealed band offsets due to Si_3N_4 - versus SiO_2 -coating of $\Delta E_C = 0.56$ eV and $\Delta E_V = 0.89$ eV. The band gap energies were $E_{\text{gap}} = 1.29$ eV for Si_3N_4 - and $E_{\text{gap}} = 1.62$ eV for SiO_2 -embedding, respectively. The shift of experimental E_C and E_V values showed band offsets of the NWells to the respective dielectric becoming more symmetric with decreasing d_{Well} . It emerged that the absolute position of E_C and E_V residing with the respective dielectric is also a function of the quantum chemical properties at the origin of the NESSIAS. The impact length for a saturation of the NESSIAS is ca. 1.5 ± 0.2 nm per plane interface, resulting in a considerable NESSIAS effect for $\leq 2.6 \pm 0.4$ nm thick Si NWells and $\leq 4.4 \pm 0.6$ nm thick Si NWires.^[3] With VLSI approaching ultrathin fins and NWires, device dimensions are currently advancing into this thickness range. It should therefore be of high interest to the

VLSI research community to carry out device-related research, in particular in the light of the prospective ultra-low power demand and low temperature functionality given by the NESSIAS effect.

4. Experimental Section

Sample Preparation: After determining the Deal-Grove parameters^[41] for the furnace oxidation of silicon-on-insulator (SOI) samples, the SOI crystalline Si (c-Si) layers (p-type, $1 \Omega\text{cm}$) on Si wafers with 145 nm buried SiO_2 (BOx) were oxidized down to a thickness of 2.1 to 6.0 nm. The SiO_2 was removed by etching in a buffered oxide etch (BOE; 1 wt-% HF buffered with NH_4F), followed by a self-limiting oxidation in 68 wt-% HNO_3 at 120 °C, yielding a 1.1 to 5.0 nm Si-NWell with 1.4 nm SiO_2 capping. A lateral metal contact frame was processed on the front surface by photolithographical structuring, wet-chemical etching in BOE for opening the top SiO_2 layer and thermal evaporation of 300 nm Al, followed by a lift-off in acetone. The Si reference samples were contacted directly on their front surface. NWell samples were coated with photo resist immediately after NWell thickness measurements using Mueller matrix ellipsometry straight after processing to prevent oxidation in air. Resist was removed just prior to sample mounting at the beamline. Si reference samples consisted of (001)-Si wafer (Sb-doped n-type, $0.01 \Omega\text{cm}$) which were treated with a BOE immediately before sample mounting under a N_2 gas flow with swift loading into the ultra-high vacuum (UHV) annealing chamber.

Si-NWells in Si_3N_4 were processed in analogy to the ones in SiO_2 , using the same SOI wafers as starting point. The SOI was thinned down to a remanent Si device layer which was 1 nm thicker than the final NWell thickness, accommodating for Si consumption during the growth of Si_3N_4 . Next, the SiO_2 capping is removed with BOE immediately before growing 3 nm of Si_3N_4 in an ammonia atmosphere by rapid thermal nitridation (RTN). Afterward, 20 nm of Si_3N_4 and 80 nm of SiO_2 were deposited by plasma enhanced chemical vapor deposition, followed by chemical mechanical polishing of the SiO_2 layer. After an RCA clean,^[42] the samples were bonded to a Si wafer^[43] covered by SiO_2 of ca. 1.5 nm thickness which was grown by an RCA-SC2 step. The original Si substrate of the SOI samples was etched back using a cyclic deep reactive ion etching process based on passivation with C_4F_8 and etching with SF_6 . The BOx served as a stopping layer and was subsequently removed by a BOE immediately before growing 1 nm of Si_3N_4 onto the remnant SOI constituting the NWell by RTN in ammonia atmosphere. Contacts to the NWells were fabricated by photolithography, locally etching the Si_3N_4 with 1 wt-% hydrofluoric acid and deposition of 300 nm Al.

The layout of the samples and a high resolution TEM image of a NWell sample is shown Figure 5.

Characterization: For synchrotron-based characterization techniques such as X-ray absorption spectroscopy measurements in total fluorescence yield (XAS-TFY) and UV photoelectron spectroscopy (UPS), all samples were subject to a UHV anneal for 60 min at 500 K to desorb water and air-related species from the sample surface prior to measurements. Synchrotron XAS-TFY measurements were carried out at the BACH CNR beamline^[44,45] at the Elettra synchrotron radiation facility in Trieste, Italy, in top-up mode at an electron energy of 2.4 GeV (140 mA electron ring current). The photon energy scale has been calibrated using the energy position of the Si L3-edge (99.6 eV) measured on a reference (001)-Si wafer. In addition, a gold (Au) layer with its 4f7/2 edge at an 87.6 eV binding energy was used as a calibration standard. A multitude of spectra was recorded per sample to obtain the data ensemble required for statistical post-processing. Further information and data on measurement parameters, measurement geometry, and statistical data post-processing can be found in the Supporting Information.

Synchrotron UPS measurements were realized at the BaDElPh beamline^[46] at the Elettra synchrotron radiation facility in Trieste, Italy, in top-up mode at an electron energy of 2.0 GeV (300 mA electron ring current). Single scans of spectra were recorded over 12 h per NWell sample and subsequently added up for eliminating white noise. Scans for the Si-reference sample were recorded over 2 h and subsequently added up. All NWell samples were excited with photon energies of initially 8.9 eV and

of 8.0 eV for subsequent measurements, and a photon flux of ca. $2 \times 10^{12} \text{ s}^{-1}$. The incident angle of the UV beam onto the sample was 50° with respect to the sample surface normal, the excited electrons were collected with an electron analyzer along the normal vector of the sample surface. Energy calibration of the UPS was realized using a tantalum (Ta) stripe in electrical contact to the sample as work function reference. Details on UPS data and measurement can be found in the Supporting Information as well as in the Supporting Information of [1] and the Appendix of [2].

The thickness of Si-NWells and its adjacent SiO_2 layers were measured using an ACCURION nanofilm ep4se ellipsometer^[47] using a Mueller matrix approach.^[48–50] Additional thickness measurements of the Si NWells and top SiO_2 were carried out by Transmission Electron Microscopy (TEM) on selected samples to confirm and/or calibrate ellipsometry measurements, see to representative NWell image in Figure 5b. All TEM samples were capped with a protective 100 nm thick SiO_2 -layer to facilitate the preparation of X-sections by the focused ion beam (FIB) technique using a FEI Strata FIB 205 workstation. Some samples were further thinned by a Fischione NanoMill. TEM analysis of the X-sections was performed at a FEI Tecnai F20 TEM operated at 200 kV at the Central Facility for Electron Microscopy, RWTH Aachen University, and at the spherical aberration corrected FEI Titan 80-300 TEM operated at 300 kV at Ernst Ruska-Centre, Forschungszentrum Jülich.^[51]

Density Functional Theory (DFT) Calculations: Real space calculations were carried out with a molecular orbital basis set (MO-BS) and Hartree–Fock (HF)/DFT methods, employing the GAUSSIAN09 program package^[52] with the GaussView program^[53] for visualization. Initially, the MO-BS wavefunction ensemble was tested and optimized for describing the energy minimum of the system (variational principle; stable = opt) with the HF method.^[54–56] Exact exchange interaction inherent to HF is crucial in obtaining accurate bond geometries, see Supporting Information of Ref.^[1] As MO-BS, we used the Gaussian type 3-21G MO-BS.^[57] This HF/3-21G route was used for the structural optimization of approximants to obtain their most stable configuration (maximum integral over all bond energies); root mean square (RMS) and peak force convergence limits were $15.3 \text{ meV } \text{Å}^{-1}$ and $23.1 \text{ meV } \text{Å}^{-1}$, (300 and $450 \mu\text{Ha}/a_{\text{B}}, o$), respectively. Optimized geometries were used to calculate their electronic structure by testing and optimizing the MO-BS wavefunction ensemble with the non-local hybrid DF B3LYP,^[58–60] its modified form featuring the Coulomb Attenuation Method (CAM-B3LYP) for more accurate asymptotic non-local exchange interactions,^[28] and the HSE06 hybrid DF with its parameters from 2006.^[27] As MO-BS, we used the Gaussian type 6-31G(d) MO-BS which contains d-polarization functions (B3LYP/6-31G(d))^[61] for all chemical elements. For all calculations, tight convergence criteria were set to the self-consistent field routine and no symmetry constraints to MOs were applied. Ultrafine integration grids were used throughout. The Supporting Information of Refs. [1] and [17] contain detailed accuracy assessments.

Supporting Information

Supporting Information is available from the Wiley Online Library or from the author.

Acknowledgements

D.K. acknowledges the 2018 Theodore-von-Kármán Fellowship of RWTH Aachen University, Germany. M.F., N.W., and J.K. acknowledge support by the Impulse and Networking Fund of the Helmholtz Association. D.H. acknowledges funding via a Heisenberg grant by the Deutsche Forschungsgemeinschaft (DFG, German Research Foundation), project #434030435. I.P., F.B., and E.M. acknowledge funding from EURO-FEL project (RoadMap Esfri) and thank Federico Salvador (IOM-CNR) for technical support. The authors acknowledge Elettra Sincrotrone Trieste for providing access to its synchrotron radiation facilities (through proposals #20165089, #20180054, #20190057, #20200079, #20205084, #20215072, and #20215081), and thank L. Sancin for technical support at

Elettra, and Simone Dal Zilio for advise and use of the Micro and Nano fabrication facility FNF at IOM-CNR. D. K. and S. C. S. acknowledge the National Computational Infrastructure (NCI) for the generous computing resources allocated on the Gadi supercomputer, Australian National University, Canberra, Australia. A small change was made to each of Equations 1, 2, S7, and S8 of this manuscript on May 12, 2023, after initial online publication. This resulted in small changes to Figure 2, which was also updated.

Conflict of Interest

The authors declare no conflict of interest.

Data Availability Statement

The data that support the findings of this study are available from the corresponding author upon reasonable request.

Keywords

electronic structure shift, NESSIAS, p/n junction, silicon nanostructures, Si_3N_4 , SiO_2 , VLSI

Received: October 13, 2022

Revised: January 6, 2023

Published online: March 18, 2023

- [1] D. König, D. Hiller, N. Wilck, B. Berghoff, M. Müller, S. Thakur, G. D. Santo, L. Petaccia, J. Mayer, S. Smith, J. Knoch, *Beilstein J. Nanotech.* **2018**, *9*, 2255.
- [2] D. König, N. Wilck, D. Hiller, B. Berghoff, A. Meledin, G. D. Santo, L. Petaccia, J. Mayer, S. Smith, J. Knoch, *Phys. Rev. Appl.* **2019**, *12*, 045050.
- [3] D. König, M. Frentzen, N. Wilck, B. Berghoff, I. Piš, S. Nappini, F. Bondino, M. Müller, S. Gonzalez, G. D. Santo, L. Petaccia, J. Mayer, S. Smith, J. Knoch, *ACS Appl. Mater. Interfaces* **2021**, *13*, 20479.
- [4] It is interesting to note in this context that current VLSI technology nodes do not reflect the physical gate length. We have a planar MOS-FET model shrunken to a size where it would perform as the fin-FET of the respective technology node, providing an implied gate length as a node index (J.-P. Collinge, Tyndall National Institute, Cork, Ireland; private communication, **2016**).
- [5] T. D. Ladd, F. Jelezko, R. Laflamme, Y. Nakamura, C. Monroe, J. L. O'Brien, *Nature* **2010**, *464*, 45.
- [6] N. Garcia-Castello, S. Illera, J. D. Prades, S. Ossicini, A. Cirera, R. Guerra, *Nanoscale* **2015**, *7*, 12564.
- [7] K. Jarolimek, E. Hazrati, R. A. de Groot, G. A. de Wijs, *Phys. Rev. Appl.* **2017**, *8*, 014026.
- [8] S. Ossicini, I. Marri, M. Amato, M. Palummo, E. Canadell, R. Rurali, *Faraday Discuss.* **2020**, *222*, 217.
- [9] S. Halilov, M. L. Belayneh, M. A. Hossain, A. A. Abdallah, B. Hoex, S. N. Rashkeev, *RSC Adv.* **2020**, *10*, 22377.
- [10] D. König, D. Hiller, S. Smith, *Phys. Stat. Sol. B* **2022**, *259*, 2100549.
- [11] B. G. Lee, D. Hiller, J.-W. Luo, O. E. Semonin, M. C. Beard, M. Zacharias, P. Stradins, *Adv. Funct. Mater.* **2012**, *22*, 3223.
- [12] N. H. Thoan, K. Keunen, V. V. Afanas'ev, A. Stesmans, *J. Appl. Phys.* **2011**, *109*, 013710.
- [13] D. K. Basaa, M. Bose, D. N. Bose, *J. Appl. Phys.* **2000**, *87*, 4324.
- [14] S. Jung, D. Gong, J. Yi, *SOLMAT* **2011**, *95*, 546.
- [15] W. Mönch, *Semiconductor Surfaces and Interfaces*, 3rd ed., Springer, Berlin **2001**.

- [16] I. H. Campbell, S. Rubin, T. A. Zawodzinski, J. D. Kress, R. L. Martin, D. L. Smith, N. N. Barashkov, J. P. Ferraris, *Phys. Rev. B* **1996**, *54*, R14321.
- [17] D. König, D. Hiller, S. Gutsch, M. Zacharias, *Adv. Mater. Interfaces* **2014**, *7*, 1400359.
- [18] D. König, J. Rudd, M. A. Green, G. Conibeer, *Phys. Rev. B* **2008**, *78*, 035339.
- [19] D. König, J. Rudd, M. A. Green, G. Conibeer, *Sol. Energy Mater. Sol. Cells* **2009**, *93*, 753.
- [20] A. F. Holleman, E. Wiberg, N. Wiberg, *Lehrbuch der Anorganischen Chemie*, Walter deGruyter, 101st ed., Berlin, **1995**, in German.
- [21] M. Scheer, R. C. Bilodeau, H. K. Haugen, *Phys. Rev. Lett.* **1998**, *80*, 2562.
- [22] Y. Guo, M. A. Whitehead, *Can. J. Chem.* **1990**, *68*, 1585.
- [23] J. E. Huheey, Ed., *Inorganic Chemistry*, 3rd ed., Harper & Row, New York **1983**, appendix 5.
- [24] A. P. Ginsberg, J. M. Miller, *J. Inorg. Nucl. Chem.* **1958**, *7*, 351.
- [25] B. Brar, G. D. Wilk, A. C. Seabaugh, *Appl. Phys. Lett.* **1996**, *69*, 2728.
- [26] N. Shirahata, J. Nakamura, J. i. Inoue, B. Ghosh, K. Nemoto, Y. Nemoto, M. Takeguchi, Y. Masuda, M. Tanaka, G. A. Ozin, *Nano Lett.* **2020**, *20*, 1491.
- [27] A. V. Krukau, O. A. Vydrov, A. F. Izmaylov, G. E. Scuseria, *J. Chem. Phys.* **2006**, *125*, 224106.
- [28] T. Yanai, D. P. Tew, N. C. Handy, *Chem. Phys. Lett.* **2004**, *393*, 51.
- [29] J. Schmidt, K. Bothe, *Phys. Rev. B* **2004**, *69*, 024107.
- [30] Bonda Technology PTE Ltd., <http://www.bondatek.com/si-wafers.html>, Accessed on January 6, 2023; search for 'Oxygen Content'.
- [31] J. R. Chelikowsky, T. J. Wagener, J. H. Weaver, A. Jin, *Phys. Rev. B* **1989**, *40*, 9644.
- [32] L. Ley, S. Kowalczyk, R. Pollack, D. A. Shirley, *Phys. Rev. Lett.* **1972**, *29*, 1088.
- [33] L. I. Schiff, *Quantum Mechanics*, 3rd ed., McGraw-Hill, Singapore **1968**, p. 39.
- [34] P. Carrier, L. J. Lewis, M. W. C. Dharma-wardana, *Phys. Rev. B* **2002**, *65*, 165339.
- [35] H. Kurata, H. Masataka, Y. Osaka, *Jap. J. Appl. Phys.* **1981**, *20*, L811.
- [36] A. Iqbal, W. B. Kackson, C. C. Tsai, J. W. Allen, C. W. Bates Jr, *J. Appl. Phys.* **1987**, *61*, 2947.
- [37] J. W. Keister, J. E. Rowe, J. J. Kolodziej, H. Niimi, T. E. Madey, G. Lucovsky, *J. Vac. Sci. Tech. B* **1999**, *17*, 1831.
- [38] E. H. Nicollian, J. R. Brews, *MOS (Metal Oxide Semiconductor) Physics and Technology*, Wiley, New York **1982**.
- [39] H. Ibach, J. E. Rowe, *Phys. Rev. B* **1974**, *10*, 710.
- [40] P. Harrison, *Quantum Wells, Wires and Dots*, 2nd ed., Wiley, Chichester, **2009**, p. 11.
- [41] B. E. Deal, A. S. Grove, *J. Appl. Phys.* **1965**, *36*, 3770.
- [42] F. W. Kern, C. A. Deckert, in *Thin Film Processes*, (Eds: V. L. Vossen, W. Kern), Academic Press, New York **1978**, pp. 411–413, Ch 5.
- [43] G. Kräuter, A. Schumacher, U. Gösele, *Sensors and Actuators A* **1998**, *70*, 271.
- [44] M. Zangrando, M. Zacchigna, M. Finazzi, D. Cocco, R. Rochow, F. Parmigiani, *Rev. Sci. Instr.* **2004**, *75*, 31.
- [45] L. Stebel, M. Malvestuto, V. Capogrosso, P. Sigalotti, B. Ressel, F. Bondino, E. Magnano, G. Cautero, F. Parmigiani, *Rev. Sci. Instr.* **2011**, *82*, 123109.
- [46] L. Petaccia, P. Vilmercati, S. Goronikov, M. Barnaba, A. Bianco, D. Cocco, C. Masciovecchio, A. Goldoni, *Nucl. Instr. Meth. in Phys. Res. A* **2009**, *606*, 780.
- [47] Nanofilm_ep4, MICROSCOPIC THIN FILM METROLOGY AND VISUALIZATION, **2020**, https://accurion.com/fileadmin/user_upload/allgemein/Accurion_Broschure_EP4_2019_optimized_web.pdf, (accessed: January 2023), see page 6 'self-assembled monolayers'.
- [48] H. Mueller, *J. Opt. Soc. Am.* **1948**, *38*, 661.
- [49] R. M. A. Azzam, *J. Opt. Soc. Am.* **1978**, *68*, 1756.
- [50] S. N. Savenkov, in *Light Scattering Reviews*, (Ed: A. A. Kokhanovsky), vol. 4, Springer, Berlin **2009**, pp. 71–119, chapter 3.
- [51] A. Thust, J. Barthel, K. Tillmann, *Journal of large-scale research facilities JLSRF* **2016**, *2*, A41.
- [52] Gaussian, Inc., Wallingford, CT, Gaussian09, Revision D.01, M. J. Frisch, et. al., **2012**, <http://gaussian.com/g09citation/>.
- [53] R. Dennington, T. Keith, J. Millam, GaussView 5.0.8, Semichem Inc., Shawnee Mission KS, **2009**.
- [54] D. R. Hartree, *Proc. Camb. Phil. Soc* **1928**, *24*, 89.
- [55] D. R. Hartree, *Proc. Camb. Phil. Soc* **1928**, *24*, 111.
- [56] V. Fock, *Zeitschr. Phys.* **1930**, *61*, 126, in German.
- [57] M. S. Gordon, J. S. Binkley, J. A. Pople, W. J. Pietro, W. J. Hehre, *J. Am. Chem. Soc.* **1982**, *104*, 2797.
- [58] A. D. Becke, *Phys. Rev. A* **1988**, *38*, 3098.
- [59] C. Lee, W. Yang, R. G. Parr, *Phys. Rev. B* **1988**, *37*, 785.
- [60] A. D. Becke, *J. Chem. Phys.* **1993**, *98*, 5648.
- [61] M. M. Francl, W. J. Pietro, W. J. Hehre, J. S. Binkley, D. J. DeFrees, J. A. Pople, M. S. Gordon, *J. Chem. Phys.* **1982**, *77*, 3654.